PAPER

Ultrathin nanoporous membranes for insulator-based dielectrophoresis

To cite this article: Hitomi Mukaibo *et al* 2018 *Nanotechnology* **29** 235704

IOP Publishing Nanotechnology

Nanotechnology 29 (2018) 235704 (10pp) https://doi.org/10.1088/1361-6528/aab5f7

Ultrathin nanoporous membranes for insulator-based dielectrophoresis

Hitomi Mukaibo (向坊 仁美)[1], Tonghui Wang[1], Victor H Perez-Gonzalez[2], Jirachai Getpreecharsawas[3], Jack Wurzer[1], Blanca H Lapizco-Encinas[4] and James L McGrath[3]

[1] Department of Chemical Engineering, University of Rochester, NY, United States of America
[2] School of Engineering and Sciences, Sensors and Devices Research Group, Tecnologico de Monterrey, NL, Mexico
[3] Department of Biomedical Engineering, University of Rochester, NY, United States of America
[4] Biomedical Engineering Department, Rochester Institute of Technology, Rochester, NY, United States of America

E-mail: hitomi.mukaibo@rochester.edu

Received 2 January 2018, revised 2 March 2018
Accepted for publication 12 March 2018
Published 10 April 2018

Abstract

Insulator-based dielectrophoresis (iDEP) is a simple, scalable mechanism that can be used for directly manipulating particle trajectories in pore-based filtration and separation processes. However, iDEP manipulation of nanoparticles presents unique challenges as the dielectrophoretic force ($\vec{F}_{DEP}$) exerted on the nanoparticles can easily be overshadowed by opposing kinetic forces. In this study, a molecularly thin, SiN-based nanoporous membrane (NPN) is explored as a breakthrough technology that enhances $\vec{F}_{DEP}$. By numerically assessing the gradient of the electric field square ($\nabla |\vec{E}|^2$)—a common measure for $\vec{F}_{DEP}$ magnitude—it was found that the unique geometrical features of NPN (pore tapering, sharp pore corner and ultrathin thickness) act in favor of intensifying the overall $\nabla |\vec{E}|^2$. A comparative study indicated that $\nabla |\vec{E}|^2$ generated in NPN are four orders of magnitude larger than track-etched polycarbonate membranes with comparable pore size. The stronger $\nabla |\vec{E}|^2$ suggests that iDEP can be conducted under lower voltage bias with NPN: reducing joule heating concerns and enabling solutions to have higher ionic strength. Enabling higher ionic strength solutions may also extend the opportunities of iDEP applications under physiologically relevant conditions. This study also highlights the effects of $\nabla |\vec{E}|^2$ induced by the ion accumulation along charged surfaces (electric-double layer (EDL)). EDL-based $\nabla |\vec{E}|^2$ exists along the entire charged surface, including locations where geometry-based iDEP is negligible. The high surface-to-volume ratio of NPN offers a unique platform for exploiting such EDL-based DEP systems. The EDL-based $\nabla |\vec{E}|^2$ was also found to offset the geometry-based $\nabla |\vec{E}|^2$, but this effect was easily circumvented by reducing the EDL thickness (e.g. increasing the ionic strength from 0.1 to 100 mM). The results from this study imply the potential application of iDEP as a direct, *in-operando* antifouling mechanism for ultrafiltration technology, and also as an active tuning mechanism to control the cut-off size limit for continuous selectivity of nanomembrane-based separations.

Keywords: insulator-based dielectrophoresis, ultrathin nanoporous membrane, numerical analysis, low voltage

(Some figures may appear in colour only in the online journal)

1. Introduction

Silicon-based nanomembranes are molecularly thin (10–100 nm) freestanding permeable membranes with pore sizes that can be tuned between 5 and 100 nm [1]. This unique structure combined with porosities as high as 40% give SiN-based nanoporous membranes (NPN) exceptional performance characteristics as platforms for biological tissue models [2, 3], as electroosmotic pumps and flow sensors [4, 5], as molecular sensors [6–8], as cell concentrators [9], and as various separation devices [1, 10–13]. A key challenge for advancing this attractive technology is to mitigate the deleterious effects of fouling—adsorption of proteins and other particles onto the nanomembrane—and improve membrane's operational life and costs [14]. The nanomembranes are particularly susceptible to clogging effects due to their extremely high permeation flux [15]. We report a theoretical study on the application of dielectrophoresis (DEP) as a direct, *in-operando* particle-trajectory manipulation mechanism for nanomembranes.

DEP is a well-known electrokinetic mechanism that is induced in polarizable particles immersed in a medium and exposed to a non-uniform electric field. The magnitude of the DEP force ($\vec{F}_{\mathrm{DEP}}$) exerted on a particle is a function of the particle and suspending medium properties, as well as the gradient of the electric field square ($\nabla |\vec{E}|^2$) [16],

$$\vec{F}_{\mathrm{DEP}} = 2\pi\varepsilon_m r^3 \mathrm{Re}\{\mathrm{CM}\}(\nabla |\vec{E}|^2), \quad (1)$$

where r is the particle radius, ε_m is the absolute permittivity of the surrounding medium and CM is the Clausius–Mossotti factor that describes the effective polarizability of the particle in the medium:

$$\mathrm{CM} = \frac{\tilde{\varepsilon}_P - \tilde{\varepsilon}_M}{\tilde{\varepsilon}_P + 2\tilde{\varepsilon}_M}, \quad \tilde{\varepsilon} = \varepsilon_r\varepsilon_0 + \frac{\sigma}{\mathrm{i}\omega}, \quad (2)$$

where ω is the frequency of the applied voltage bias, and subscripts P and M represent the particle and the medium, respectively, σ is the conductivity, and i is the imaginary number. The above equations indicate that the $\vec{F}_{\mathrm{DEP}}$ exerted on a particle can be controlled by simply tuning the frequency or the magnitude of the applied voltage [16–18]. When the value of Re{CM} is positive, particles migrate towards stronger electric-field regions (positive DEP), and when Re{CM} is negative, particles move away from stronger electric-field regions (negative DEP) [19]. When ε_m, r, and CM are constant, $\vec{F}_{\mathrm{DEP}}$ becomes proportional to $\nabla |\vec{E}|^2$—a value commonly used as a measure of $\vec{F}_{\mathrm{DEP}}$ magnitude in numerical analyses [20].

Generating $\nabla |\vec{E}|^2$, and thus $\vec{F}_{\mathrm{DEP}}$ on particles, by focusing electric field across pore orifices of insulating porous membranes is one type of commonly studied insulator-based DEP (or iDEP) systems [9, 21, 22]. Employing negative DEP forces drives particles away from the pore orifice, offering a simple, scalable mechanism for manipulating particle trajectory in pore-based separation/filtration systems [9, 23–28]. However, application of iDEP to manipulate nanoparticles is challenging due to the presence of other opposing kinetic forces—such as electroosmotic flow (EOF), electrophoresis (EP), convection and/or Brownian motion—that can easily overshadow $\vec{F}_{\mathrm{DEP}}$ exerted on nm-scale particles. Larger $\vec{F}_{\mathrm{DEP}}$ are commonly achieved by increasing the applied voltage from tens of volts to thousands of volts, but such high voltages cause rapid Joule heating that alter the electrokinetic forces acting on the particle and lower the energy efficiency of the process [29–36].

This study was motivated by the hypothesis that the unique nm-scale geometry of nanomembranes will lower the ohmic losses and enhance the field-focusing effect at the pore orifice. Key parameters that affect $\vec{F}_{\mathrm{DEP}}$ are identified by COMSOL® numerical analyses. The results indicate that the nanomembrane geometry has the potential to increase $\vec{F}_{\mathrm{DEP}}$ by four orders of magnitude compared to commercial track-etch polycarbonate (TEPC) membranes with comparable pore size. The study also showed that $\vec{F}_{\mathrm{DEP}}$ generated in NPN geometries are susceptible to $\nabla |\vec{E}|^2$ induced by electrical double layer (EDL). The EDL-induced $\nabla |\vec{E}|^2$ fields are concentration dependent, cover the entire charged surfaces, and may affect the $\nabla |\vec{E}|^2$ induced by the geometric effect.

2. Methods

2.1. Numerical model

A two-dimensional (2D) axial symmetric model of a single nanopore in a membrane was developed to analyze the induced $\nabla |\vec{E}|^2$ (figure 1). The axial symmetry boundary was set at $r = 0$. The dimensions of the nanopore are defined by the pore tip radius (r_p), pore taper angle (θ), radius of curvature at the edge of the pore opening (r_c) and the thickness of the membrane (H). To evaluate the magnitude of steady-state $\nabla |\vec{E}|^2$, an arbitrary electric potential ($\phi_{\mathrm{app}} = 1$ V) is placed 20 μm above the top surface of the membrane ($z = 0$) and the ground (0 V) is placed 20 μm below the bottom surface of the membrane ($z = -H$). The radial boundary of the fluid (i.e., the membrane and the electrode radii) were 10 μm. Ample height and radius was given to the fluid reservoir (relative to the pore radius (~15 nm)) to ensure minimal effect of the fluid reservoir size on the electric field distribution. All other boundaries (red and green lines, figure 1) are defined as electrically insulating.

The relative permittivity of water ($\varepsilon_w = 78.5$) and aqueous solution conductivity of either 0.1 mM NaCl (14.45 μS cm^{-1}, measured experimentally) or 100 mM NaCl (10 mS cm^{-1}, interpolated from [37]) was used for the fluid property. Details of the domains and boundary equations applied to solve our computational model are given in table 1.

The Poisson equation was used to relate the local charge density to the electrostatic potential, and the Nernst–Planck equation was used to describe the contribution of diffusion, EP and EOF to the ionic species distribution [38, 39]. The model was calculated assuming steady-state with no convection effects, and both equations were coupled during the analyses.

The ions were assumed to be monovalent, with diffusivity of 1×10^{-9} m^2 s^{-1}. The initial concentration and the concentration at the two electrodes (boundaries 1 and 2 in

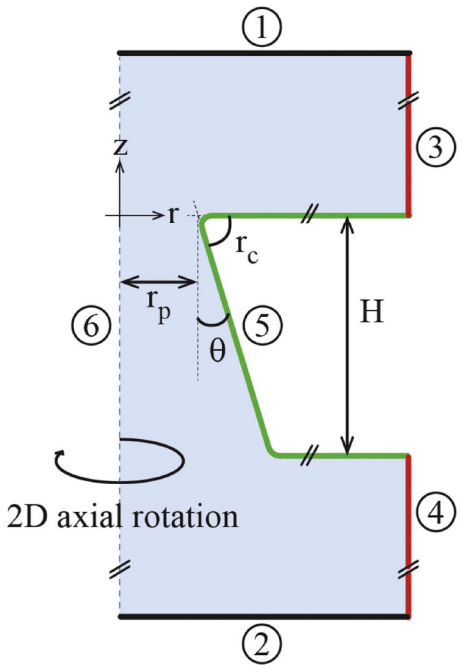

Figure 1. Schematic representation of the 2D axial symmetry model (half of a pore). The parameters r_p, θ, r_c and H represent the pore tip radius, pore taper angle, radius of curvature at the edge of pore opening, and the thickness of the membrane, respectively. The blue region represents the fluid domain, the green line indicates the surface boundary of the membrane, the red lines indicate the radial boundary of the fluid, and the black lines indicate the surface boundary of the electrodes. The numbers indicate the boundary labels used to define the computational model in table 1.

figure 1) were defined to be equal to the bulk concentration (0.1 or 100 mM).

2.2. Cross-sectional scanning electron microscopy (SEM) imaging

A 6 μm thick TEPC membrane (Sterlitech) was first photo-oxidized by exposure to UV light ($\lambda = 185$ nm, Novascan Technologies, Ames, Iowa, USA) for 11 h. Photo-oxidation made the TEPC membrane brittle, preventing membrane deformation during the fracturing process [40]. The NPN (SiMPore, West Henrietta, NY, USA) is naturally brittle and could be fractured without prior treatment. Both fractured membranes were mounted on a stub using a conductive tape, and then sputter-coated (Denton Vacuum, Moorestown, NJ, USA) with platinum at 15 mA and 100 mTorr for 80 s. The final thickness of the sputtered platinum was about 8 nm. The SEM images were obtained at 15 kV (ZEISS, Thornwood, NY, USA).

3. Results and discussion

3.1. Pore geometry considered for the numerical model

The pore dimensions considered in the numerical model (figures 2(a) and (c)) were based on averages of several measurements taken from cross-sectional SEM images of TEPC membrane and NPN with comparable pore diameters (figures 2(b) and (d)). The NPN modeled in this study is 120 times thinner than the TEPC membrane, has conical pores instead of cylindrical pores, and has a much sharper pore corner.

3.2. Effect of pore geometry on electric field distribution

The discussion in this section is focused on the effect of nm-scale membrane geometry on the magnitude and coverage of $\nabla |\vec{E}|^2$ at and around the pore orifice ($z \approx 0$). This study considers that all particles will exhibit negative dielectrophoretic behavior and are repelled from the pore orifice. This is a reasonable assumption as it can be accomplished through careful selection of the voltage frequency and suspending medium conductivity. Smaller magnitudes of $\nabla |\vec{E}|^2$ correspond to weaker repulsive $\vec{F}_{\mathrm{DEP}}$, which increases the probability for particles to slip into the pore and/or foul the nanoporous membrane. It is critical that a wide coverage of strong $\nabla |\vec{E}|^2$ is generated at and around the pore orifice to achieve the effective manipulation of nanoparticle trajectories.

Figure 3 illustrates the 2D distribution of $\nabla |\vec{E}|^2$ at the vicinity of a pore orifice for different pore geometries. Figure 3(a) shows that the magnitude of $\nabla |\vec{E}|^2$ increases significantly with decreasing membrane thickness: at $H = 10$ nm, strong $\nabla |\vec{E}|^2$ fills the entire pore (figure 3(a), left), while at $H = 10\,000$ nm, $\nabla |\vec{E}|^2$ is too small to be imaged with the given color scale (figure 3(a), right). The image for $H = 100$ nm (figure 3(a), center) shows the typical distribution trend for $\nabla |\vec{E}|^2$ induced by an axial-symmetrical pore geometry: the $\nabla |\vec{E}|^2$ is stronger at the pore edge where the electric field is intensely perturbed (as illustrated in red color), and is weaker along the pore center ($r = 0$) where the electric field is less perturbed [41, 42]. Figure 3(b) shows that tapered (or conical) pores result in stronger $\nabla |\vec{E}|^2$ compared to cylindrical pores. This is attributed to the 'field-focusing effect' of tapered pores that is well-known in single-nanopore membrane studies [38, 43] and iDEP studies in tapered geometries [44, 45]. Figure 3(c) studies the effect of radius of curvature which is also a well-known attribute in affecting $\nabla |\vec{E}|^2$ of iDEP systems [20]. It is interesting to note that larger curvature not only weakens $\nabla |\vec{E}|^2$, but also shifts the location of strong $\nabla |\vec{E}|^2$ deeper into the pore (figure 3(c), left)—leaving the pore opening more susceptible to particle adsorption and accumulation.

Figure 4 is a quantitative representation of the relative effect of the three pore geometric variables (H, θ, and r_c) shown in figure 3. Defining the maximum $\nabla |\vec{E}|^2$ at $z = 0$ as $\nabla |\vec{E}|^2_{\mathrm{max}}$, the '*Relative* $\nabla |\vec{E}|^2_{\mathrm{max}}$' at each variable is calculated as the relative magnitude of $\nabla |\vec{E}|^2_{\mathrm{max}}$ with respect to the smallest $\nabla |\vec{E}|^2_{\mathrm{max}}$ in the figure. For example, the smallest $\nabla |\vec{E}|^2_{\mathrm{max}}$ in figure 4(a) is at $H = 10\,000$ nm. Therefore, *Relative* $\nabla |\vec{E}|^2_{\mathrm{max}}$ for a membrane that is x nm thick is

Table 1. Domain and boundary conditions used in the computational model.

	Domain/boundary (see figure 1)	Equation
The electostatics interface		
Charge conservation	Blue	$\vec{E} = -\nabla\phi$ $\nabla \cdot (\varepsilon_0 \varepsilon_W \vec{E}) = \rho_v$ $\vec{D} = \varepsilon_0 \varepsilon_W \vec{E}$
Axial symmetry	6	N/A
Zero charge	3, 4	$\vec{n} \cdot \vec{D} = 0$
Space charge density	Blue	$\nabla \cdot \vec{D} = \rho_v$
Surface charge density	5	$\vec{n} \cdot (\overrightarrow{D_1} - \overrightarrow{D_2}) = \rho$
Ground	2	$\phi = 0$
Electric potential	1	$\phi = \phi_{app}$
The Nernst–Planck equation interface		
Transport properties	Blue	$\nabla \cdot (-D_i \nabla c_i - z_i u_{m,i} F c_i \nabla\phi) = 0$ $\overrightarrow{N_i} = -D_i \nabla c_i - z_i u_{m,i} F c_i \nabla\phi$
Axial symmetry	6	N/A
No flux	5	$-\vec{n} \cdot \overrightarrow{N_i} = 0$
Concentration	1, 2	$c_i = c_{0,i}$
Symmetry		$-\vec{n} \cdot \overrightarrow{N_i} = 0$

Note. Where $\vec{E}$ is the electric field, ϕ is the electric potential field, ε_0 is the permittivity of free space, $\vec{D}$ is the electric flux density, $\vec{n}$ is a normal vector, $\vec{D_1}$ and $\vec{D_2}$ are the electric flux density of water and membrane surface, respectively, ρ_v is the volume charge density, D_i is the diffusivity coefficient for the ith ionic species, c_i is the concentration of the ith ionic species, $c_{0,i}$ is the initial concentration of the ith ionic species, z_i is the charge number of the ith ionic species, $u_{m,i}$ is the ionic mobility of the ith ionic species, and F is Faraday's constant.

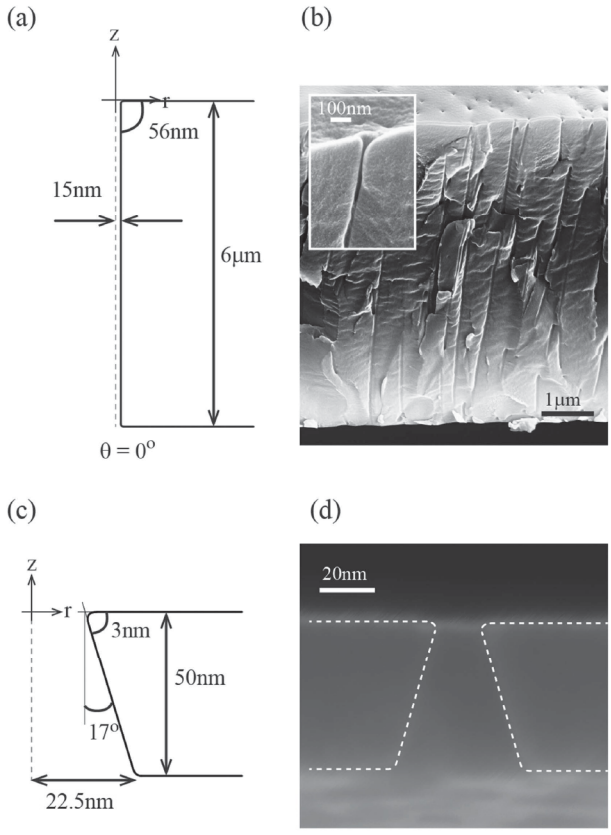

Figure 2. (a) Illustration of the pore geometry used in the numerical model for the TEPC membrane and (b) representative SEM image of the cross-section of a TEPC membrane. (c) Illustration of the pore geometry used in the numerical model for the NPN and (d) representative SEM image of the cross-section of an NPN. The dimensions in the numerical models for both membranes are average values of the dimensions measured from representative SEM images.

calculated as:

$$\frac{(\text{Relative } \nabla |\vec{E}|^2_{\max} \text{ at } H = x \text{ nm})}{(\nabla |\vec{E}|^2_{\max} \text{ at } H = x \text{ nm})} = \frac{(\nabla |\vec{E}|^2_{\max} \text{ at } H = x \text{ nm})}{(\nabla |\vec{E}|^2_{\max} \text{ at } H = 10\,000 \text{ nm})}. \quad (3)$$

Figure 4(a) shows that the Relative $\nabla |\vec{E}|^2_{\max}$ increased by a factor of ~90 000 by reducing the membrane thickness from 10 000 nm (comparable to TEPC membrane) to 10 nm (comparable to NPN). The almost linear increase in intensity (illustrated by the dotted line) with decreasing membrane thickness can be attributed to the linear drop in ohmic resistance with thinner membranes. Deviation from the linearity that starts around $H = 100$ nm is attributed to the overlap of $\nabla |\vec{E}|^2$ from the top and the bottom of the membrane, as shown in figure 3(a) (left).

Our numerical analyses also indicate that a three orders of magnitude increase in Relative $\nabla |\vec{E}|^2_{\max}$ can be achieved with just 5° tapering of the pore (figure 4(b)). At $\theta = 20°$, the Relative $\nabla |\vec{E}|^2_{\max}$ was four orders of magnitude larger than that of cylindrical pores ($\theta = 0°$). Figure 4(c) shows that Relative $\nabla |\vec{E}|^2_{\max}$ drops by an order of magnitude as r_c increases from 3° to 10°. As shown in figure 3(c), this is because the location of $\nabla |\vec{E}|^2$ shifts deeper into the pore with larger r_c. For all variables studied here (H, θ, and r_c) it was found that $\nabla |\vec{E}|^2$ along the centerline of the pore (the location with the weakest $\nabla |\vec{E}|^2$ within the pore) was larger for cases with larger Relative $\nabla |\vec{E}|^2_{\max}$. This is important because it indicates that the geometry-based $\nabla |\vec{E}|^2$ enhancement not only intensifies $\vec{F}_{DEP}$, but also decreases the chance of particles slipping through the locations with relatively lower $\vec{F}_{DEP}$.

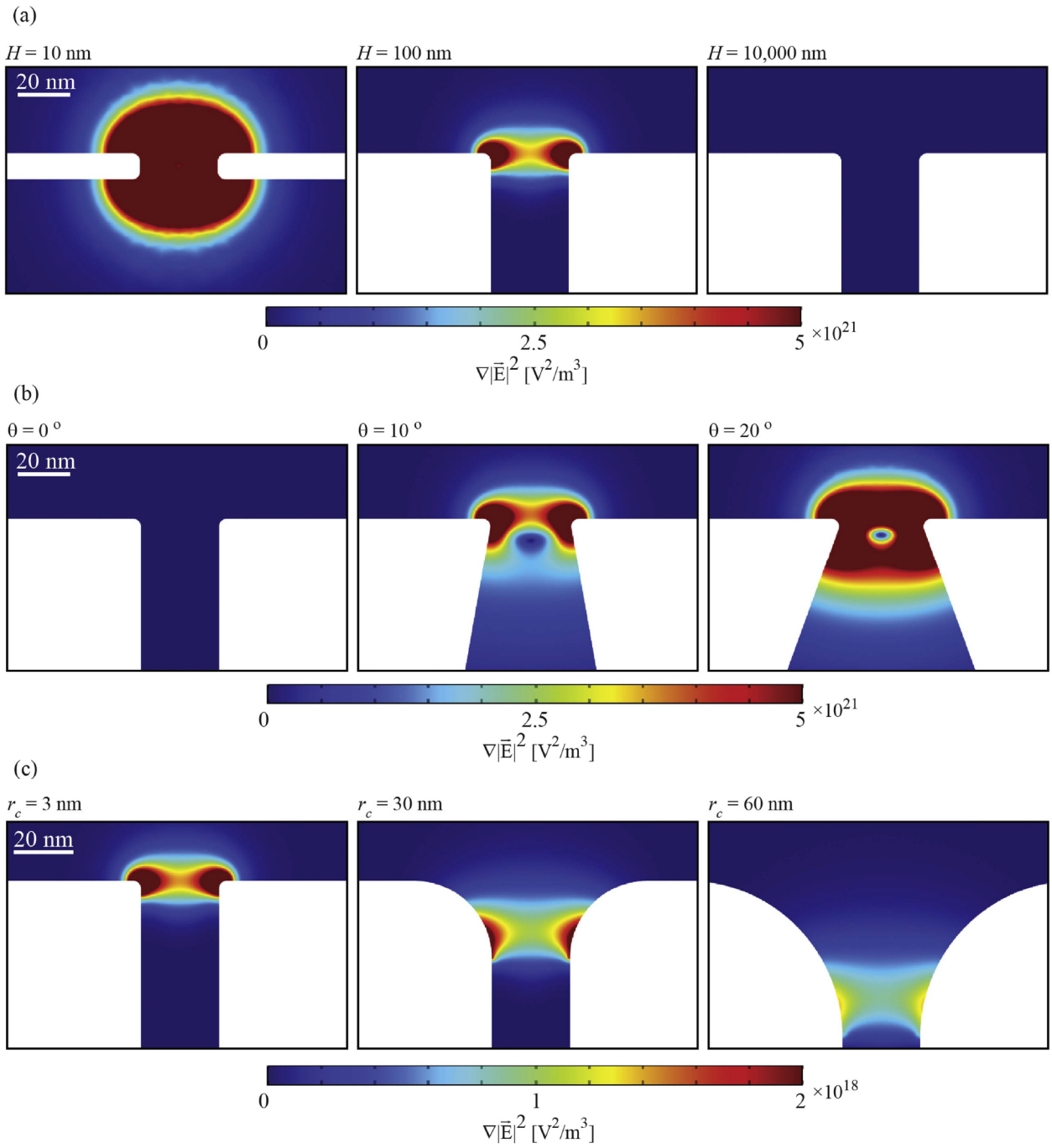

Figure 3. 2D COMSOL® image of the spatial distribution of $\nabla |\vec{E}|^2$ at the vicinity of the pore opening. Each row illustrates the effects of (a) membrane thickness, H, (b) pore tapering, θ, and (c) radius of curvature at pore corner, r_c. Unless treated as a variable, H, θ, r_c and r_p are 6 μm, 0°, 3 nm, and 15 nm, respectively, for all calculations.

Both figures 3 and 4 indicate that all the key geometrical features of the NPN (ultrathin, tapered pore with small radius of curvature) act in favor of inducing stronger negative $\vec{F}_{\mathrm{DEP}}$ on the particles than what was available using conventional nanoporous membranes (e.g. TEPC membranes). Indeed, when $\nabla |\vec{E}|^2$ induced with conventional TEPC (figure 2(b)) and NPN (figure 2(c)) geometries are compared (figure 5), the maximum $\nabla |\vec{E}|^2$ along the surface ($z = 0$) of the NPN model was found to be around four orders of magnitude stronger than that of the TEPC model. The results in figure 5 are clear evidence that NPN combined with iDEP offer an attractive opportunity to realize tunable antifouling membrane processes.

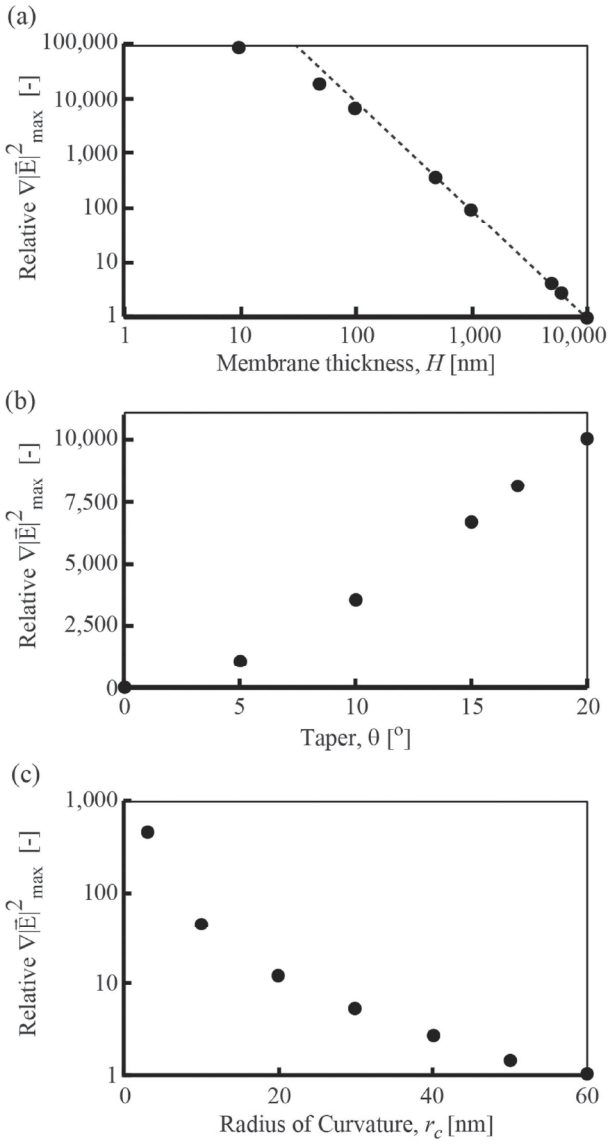

Figure 4. Effect of pore geometry on relative $\nabla|\vec{E}|^2_{max}$: (a) membrane thickness, H, (b) pore tapering, θ, and (c) radius of curvature at pore corner, r_c. The dotted line in (a) is added to illustrate the linear region of the plot. Unless treated as a variable, H, θ, r_c and r_p are 6 μm, 0°, 3 nm, and 15 nm, respectively, for all calculations.

3.3. Effect of EDL on $|\vec{E}|^2$

It has been shown that NPN possesses a negative surface charge [46], which accumulates cations at its surface (i.e. EDL formation) [5]. The discussion in this section is focused on the effect of the cationic EDL on $\nabla|\vec{E}|^2$. An NPN model with surface charge density of $-1\ \mu C\,cm^{-2}$ [47] was compared to a hypothetical model with no surface charge, and an intermediate surface charge of $-0.5\ \mu C\,cm^{-2}$ (figure 6). Figure 6(a) compares the concentration of cations under three different surface charge density (ρ) magnitudes. At zero surface charge, the ion concentration in the solution is uniform at its bulk concentration (0.1 mM). As expected, higher

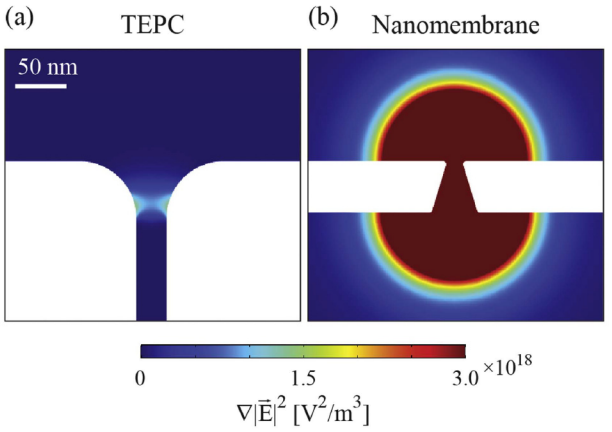

Figure 5. Illustration of the 2D distribution of $\nabla|\vec{E}|^2$. In a pore using (a) TEPC model and (b) NPN model (figure 2).

accumulation of cation is observed at surfaces with larger ρ magnitude. Considering that a positive voltage bias is placed above the smaller pore orifice (tip), it may seem counter-intuitive that cation concentration is higher at the tip than at the base (larger pore orifice). This is because the cationic EDL starts to overlap as the pore radius becomes smaller, and forms a cation-rich region around the tip opening [38, 48]. When the same numerical analyses are repeated for a cylindrical pore with the radius of the base opening ($\theta = 0°$, $r_p = 22.5$ nm), the cation concentration is higher at the base, away from the positive electric bias (data not shown). Anion and cation distributions within the nanopore can be tuned by controlling the EDL thickness, the electric field imposed by the electrodes and the sign (positive or negative) of the membrane surface charge.

The effect of surface charge density on the magnitude and distribution of $\nabla|\vec{E}|^2$ (figure 6(b)) highlights a unique feature of nm-scale geometries: EDL can have a significant effect on the geometry-induced $\nabla|\vec{E}|^2$. In micron-scale geometries, EDL formation has a negligible effect on iDEP because the EDL thickness can be assumed to be negligible when compared to the pore radius. However, in nm-scale pores, the dimensions of EDL may become comparable to the pore radius and exhibit significant effect on the electric-field distribution (and hence the $\nabla|\vec{E}|^2$) within the pore. The left figure in figure 6(b), at zero surface charge, illustrates the $\nabla|\vec{E}|^2$ generated purely by the NPN geometry. Strong and focused $\nabla|\vec{E}|^2$ is observed at and around the tip opening. In contrast, $\nabla|\vec{E}|^2$ is less focused and more distributed for models with surface charge (figure 6(b), center and right). This is because the cations accumulated around the pore tip screens and cancels the $\nabla|\vec{E}|^2$ generated by the geometry. The magnitude of $\nabla|\vec{E}|^2$ was partially restored by increasing the surface charge density from -0.5 to $-1\ \mu C\,cm^{-2}$.

Another, perhaps more interesting, observation from figure 6(b) is the appearance of $\nabla|\vec{E}|^2$ along the flat surface of membranes when the surface charge is non-zero. This is again attributed to the accumulation of cations in EDL (figure 6(a)), which results in electric field non-uniformities at

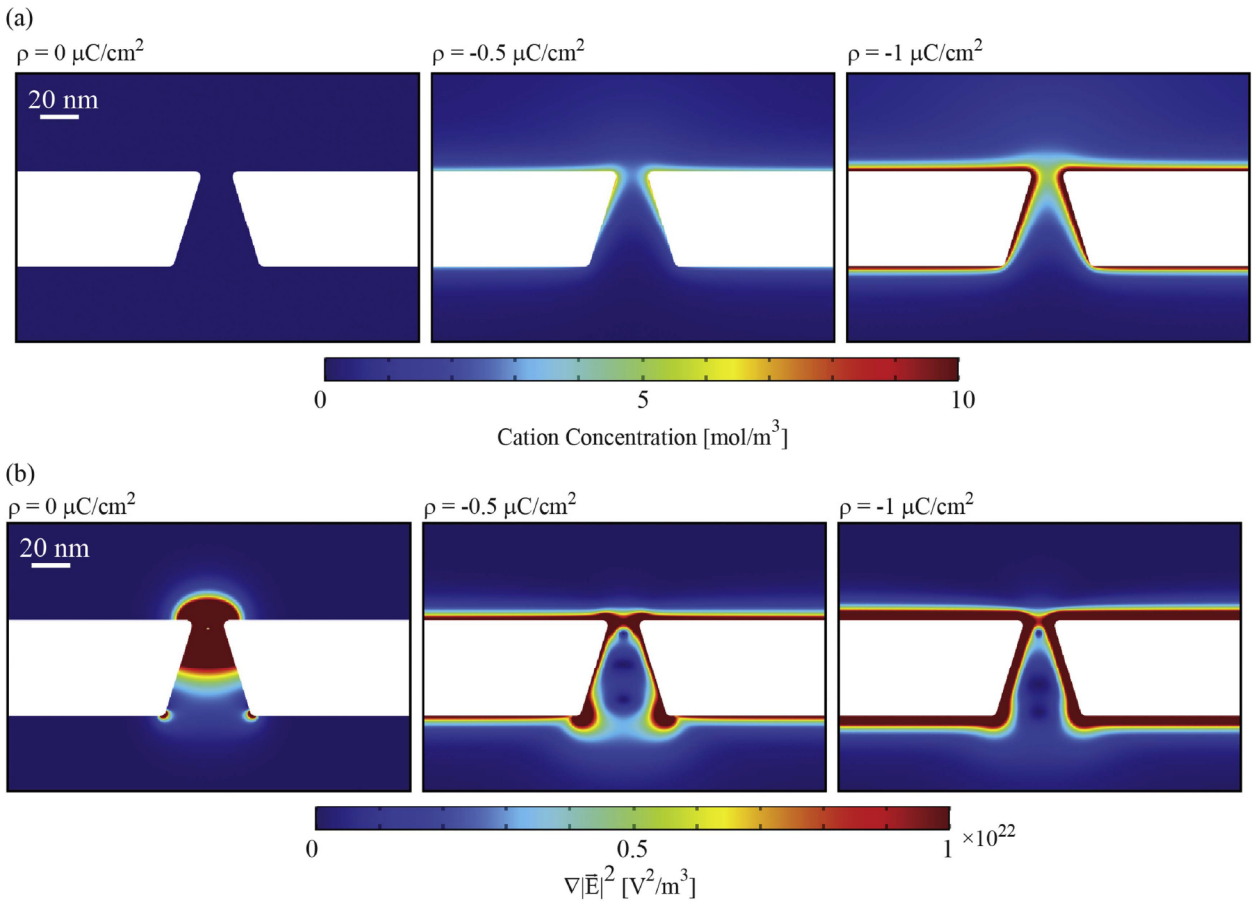

Figure 6. Effect of surface charge on (a) cation distribution and (b) $\nabla |\vec{E}|^2$ distribution. The dimensions of the model is as shown in figure 2(c). Bulk concentration was 0.1 mM.

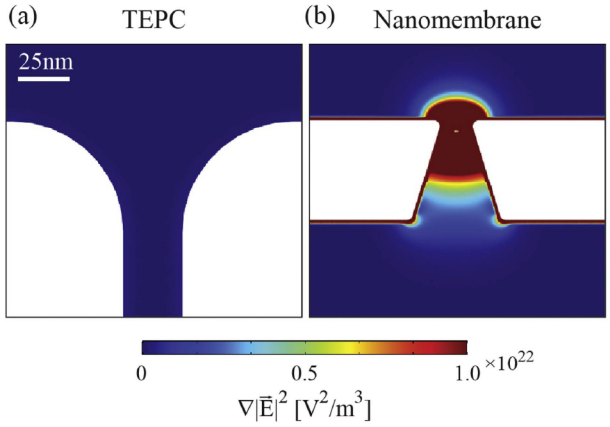

Figure 7. Illustration of 2D images of (a) $\nabla |\vec{E}|^2$ distribution using a TEPC geometry with surface charge of $-0.2\ \mu C\ cm^{-2}$, and (b) NPN geometry with surface charge of $-1\ \mu C\ cm^{-2}$. The bulk salt concentration is 100 mM.

the membrane surface regardless of position. Without surface charge, $\nabla |\vec{E}|^2$ diminishes rapidly beyond the pore opening (figure 6(b), left). These EDL-based $\nabla |\vec{E}|^2$ do not depend on the applied voltage bias but on the concentration gradient of the cations within the EDL, which is a function of surface charge density, ion concentration, and ion species [49]. At higher surface charge density, the ion concentration gradient within the EDL increases, which results in larger $\nabla |\vec{E}|^2$, as shown in figure 6(b) (center and right).

The above discussion also indicates that the effect of EDL-based $\nabla |\vec{E}|^2$ on the geometric field-focusing based $\nabla |\vec{E}|^2$ can easily be manipulated by modifying the thickness of the EDL. Figure 7 demonstrates this concept, where the thickness of EDL—being inversely proportional to the square root of concentration [49]—is reduced by increasing the salt concentration from 0.1 mM (in figure 6) to 100 mM. The figure shows a thin, dark red layer around the entire surface of the nanomembrane indicating strong $\nabla |\vec{E}|^2$ due to EDL. The EDL thickness is much thinner than the pore radius, allowing for a strong geometric field-focusing based $\nabla |\vec{E}|^2$ to develop around the pore orifice without being significantly cancelled by the cationic EDL. Compared with the $\nabla |\vec{E}|^2$ induced from conventional TEPC model (figure 7(a)) [50], the NPN model shows significantly stronger $\nabla |\vec{E}|^2$ at the pore opening (figure 7(b)). The numerical analyses estimated the maximum $\nabla |\vec{E}|^2$ along the surface ($z = 0$) of the NPN model to be ~3000 times stronger than that of the TEPC model.

Finally, it is important to note that a particle with diameter comparable to (or larger than) the membranes' pore

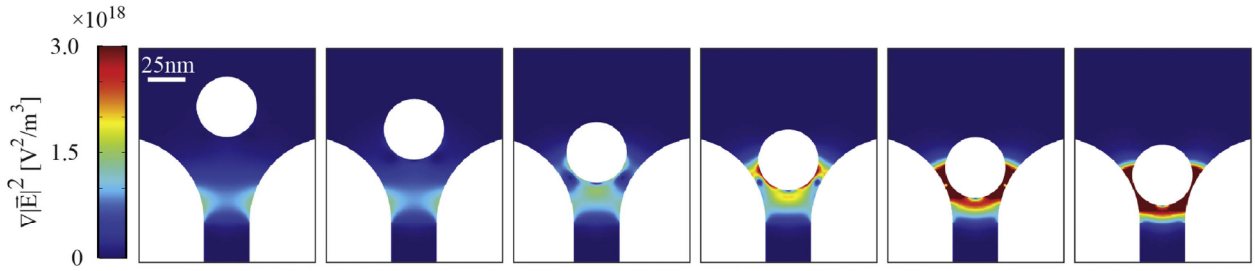

Figure 8. Illustration of $\nabla |\vec{E}|^2$ for a 20 nm radius particle placed at varying distances above and within a 15 nm radius pore opening. The TEPC model was used for the analyses, and effects of surface charge are neglected in these models.

diameter will experience increasing $\nabla |\vec{E}|^2$ intensity as it approaches the pore opening [26, 51]. This concept is illustrated in figure 8, which shows the numerical analyses of $\nabla |\vec{E}|^2$ when an insulating particle is placed at varying distances from a TEPC pore opening. This suggests that nanoparticles experience an even larger negative $\vec{F}_{\mathrm{DEP}}$ at NPN pore orifice than those predicted in figures 3–7. In combination with the EDL-based $\nabla |\vec{E}|^2$ that covers the entire area of a charged surface, iDEP offers an appealing opportunity for NPN as a potential mechanism for antifouling and/or tunable particle size-separation process.

4. Conclusions

The objective of this study was to explore the unique nm-scale geometry of insulating NPN on the magnitude of DEP. $\nabla |\vec{E}|^2$ was numerically estimated as a representative measure of the iDEP force. As a result, geometry-based $\nabla |\vec{E}|^2$ was found to increase by almost five orders of magnitude when the thickness of a porous membrane was decreased from 10 000 nm (comparable to conventional systems) to 10 nm (comparable to NPN systems). Furthermore, the extra sharp pore corners and tapering of the pores—based on NPN cross-sectional images—were also found to be significantly beneficial in increasing geometry-based $\nabla |\vec{E}|^2$. The stronger $\nabla |\vec{E}|^2$ suggests that iDEP can be conducted under lower voltage bias with NPN: reducing joule heating concerns and enabling solutions to have higher ionic strength. Enabling higher ionic strength solutions may also extend the opportunities of iDEP applications under physiologically relevant conditions.

The analyses also highlighted the effect of cationic EDL, where non-uniform distribution of cations along the negatively-charged surface induced $\nabla |\vec{E}|^2$ at locations where conventional geometrical iDEP is considered negligible (e.g. along flat surfaces). This may offer a novel approach for manipulating particle trajectories using DEP with only surface and solution properties, and zero voltage biases. The NPN with high surface-to-volume ratio would be one of the ideal platforms for taking full advantage of such surface-charge-based DEP systems. The EDL also had undesirable effects of significantly reducing the geometry-based $\nabla |\vec{E}|^2$ at the vicinity of pore orifice, especially when the relative thickness of EDL is comparable to pore radius. This effect can be minimized by additional, practical strategies that decrease EDL thickness, such as increasing salt concentration, increasing the valence of the ions, or decreasing the surface charge density of NPN.

Although the comparative discussion is limited to membranes with identical porosity (number of pores per unit area), this work lays the foundation for exploring iDEP as an *in-operando* mechanism for manipulating nanoparticle trajectories at nanoporous membranes. Successful incorporation of iDEP into the ultrafiltration technology will enable a groundbreaking approach for membrane antifouling, as well as for actively tuning the cut-off size limit: a novel mechanism for continuous selectivity of nanomembrane-based separations.

Acknowledgment

The authors would like to acknowledge the financial support provided by the National Science Foundation (Award CBET-1705895).

ORCID iDs

Hitomi Mukaibo (向坊 仁美) https://orcid.org/0000-0001-7195-6403
Victor H Perez-Gonzalez https://orcid.org/0000-0003-4503-7774

References

[1] Striemer C C, Gaborski T R, McGrath J L and Fauchet P M 2007 Charge- and size-based separation of macromolecules using ultrathin silicon membranes *Nature* **445** 749–53
[2] Nehilla B J, Nataraj N, Gaborski T R and McGrath J L 2014 Endothelial vacuolization induced by highly permeable silicon membranes *Acta Biomater.* **10** 4670–7
[3] Mazzocchi A R, Man A J, DesOrmeaux J-P S and Gaborski T R 2014 Porous membranes promote endothelial differentiation of adipose-derived stem cells and perivascular interactions *Cell. Mol. Bioeng.* **7** 369–78
[4] Getpreecharsawas J, McGrath J L and Borkholder D A 2015 The electric field strength in orifice-like nanopores of ultrathin membranes *Nanotechnology* **26** 045704

[5] Snyder J L, Getpreecharsawas J, Fang D Z, Gaborski T R, Striemer C C, Fauchet P M, Borkholder D A and McGrath J L 2013 High-performance, low-voltage electroosmotic pumps with molecularly thin silicon nanomembranes *Proc. Natl Acad. Sci. USA* **110** 18425–30

[6] Kavalenka M N, Striemer C C, DesOrmeaux J-P S, McGrath J L and Fauchet P M 2012 Chemical capacitive sensing using ultrathin flexible nanoporous electrodes *Sensors Actuators* B **162** 22–6

[7] Hirohito Y, Keiko E and Toshiharu S 2017 A 150 nm ultraviolet excitation volume on a porous silicon membrane for direct optical observation of DNA coil relaxation during capture into nanopores *Nano Futures* **1** 011001

[8] Briggs K, Madejski G, Magill M, Kastritis K, de Haan H W, McGrath J L and Tabard-Cossa V 2017 DNA translocations through nanopores under nanoscale preconfinement *Nano Lett.* **18** 660–8

[9] Cho Y-K, Kim S, Lee K, Park C, Lee J-G and Ko C 2009 Bacteria concentration using a membrane type insulator-based dielectrophoresis in a plastic chip *Electrophoresis* **30** 3153–9

[10] Gaborski T R, Snyder J L, Striemer C C, Fang D Z, Hoffman M, Fauchet P M and McGrath J L 2010 High-performance separation of nanoparticles with ultrathin porous nanocrystalline silicon membranes *ACS Nano* **4** 6973–81

[11] DesOrmeaux J P S, Winans J D, Wayson S E, Gaborski T R, Khire T S, Striemer C C and McGrath J L 2014 Nanoporous silicon nitride membranes fabricated from porous nanocrystalline silicon templates *Nanoscale* **6** 10798–805

[12] Snyder J L, Clark A Jr, Fang D Z, Gaborski T R, Striemer C C, Fauchet P M and McGrath J L 2011 An experimental and theoretical analysis of molecular separations by diffusion through ultrathin nanoporous membranes *J. Membr. Sci.* **369** 119–29

[13] Ishimatsu R, Kim J, Jing P, Striemer C C, Fang D Z, Fauchet P M, McGrath J L and Amemiya S 2010 Ion-selective permeability of an ultrathin nanoporous silicon membrane as probed by scanning electrochemical microscopy using micropipet-supported ITIES tips *Anal. Chem.* **82** 7127–34

[14] Goosen M, Sablani S S, Al-Hinai H, Al-Obeidani S, Al-Belushi R and Jackson D 2004 Fouling of reverse osmosis and ultrafiltration membranes: a critical review *Sep. Sci. Technol.* **39** 2261–97

[15] Winans J D, Smith K J P, Gaborski T R, Roussie J A and McGrath J L 2016 Membrane capacity and fouling mechanisms for ultrathin nanomembranes in dead-end filtration *J. Membr. Sci.* **499** 282–9

[16] Jones T B 1995 *Electromechanics of Particles* (Cambridge: Cambridge University Press)

[17] Pethig R 2010 Review article—dielectrophoresis: status of the theory, technology, and applications *Biomicrofluidics* **4** 022811

[18] Gascoyne P R C and Vykoukal J 2002 Particle separation by dielectrophoresis *Electrophoresis* **23** 1973–83

[19] Morgan H and Green N G 2003 *AC Electrokinetics: Colloids and Nanoparticles* (Baldock, Hertfordshire: Research Studies Press) p 324

[20] Pesch G R, Kiewidt L, Du F, Baune M and Thöming* J 2016 Electrodeless dielectrophoresis: impact of geometry and material on obstacle polarization *Electrophoresis* **37** 291–301

[21] Nakano A and Ros A 2013 Protein dielectrophoresis: advances, challenges, and applications *Electrophoresis* **34** 1085–96

[22] Regtmeier J, Eichhorn R, Viefhues M, Bogunovic L and Anselmetti D 2011 Electrodeless dielectrophoresis for bioanalysis: theory, devices and applications *Electrophoresis* **32** 2253–73

[23] Lin I J and Benguigui L 1982 High-intensity, high-gradient electric separation and dielectric filtration of particulate and granular materials *J. Electrost.* **13** 257–78

[24] Hakoda M 2016 Development of dielectrophoresis separator with an insulating porous membrane using DC-offset AC electric fields *Biotechnol. Prog.* **32** 1292–300

[25] Pesch G R, Du F, Schwientek U, Gehrmeyer C, Maurer A, Thoeming J and Baune M 2014 Recovery of submicron particles using high-throughput dielectrophoretically switchable filtration *Sep. Purif. Technol.* **132** 728–35

[26] Du F, Ciaciuch P, Bohlen S, Wang Y, Baune M and Thöming J 2013 Intensification of cross-flow membrane filtration using dielectrophoresis with a novel electrode configuration *J. Membr. Sci.* **448** 256–61

[27] Du F, Hawari A, Baune M and Thoeming J 2009 Dielectrophoretically intensified cross-flow membrane filtration *J. Membr. Sci.* **336** 71–8

[28] Du F, Hawari A H, Larbi B, Ltaief A, Pesch G R, Baune M and Thöming J 2018 Fouling suppression in submerged membrane bioreactors by obstacle dielectrophoresis *J. Membr. Sci.* **549** 466–73

[29] Nakano A, Luo J and Ros A 2014 Temporal and spatial temperature measurement in insulator-based dielectrophoretic devices *Anal. Chem.* **86** 6516–24

[30] Gallo-Villanueva R C, Sano M B, Lapizco-Encinas B H and Davalos R V 2014 Joule heating effects on particle immobilization in insulator-based dielectrophoretic devices *Electrophoresis* **35** 352–61

[31] Xuan X 2008 Joule heating in electrokinetic flow *Electrophoresis* **29** 33–43

[32] Petersen N J, Nikolajsen R P H, Mogensen K B and Kutter J P 2004 Effect of joule heating on efficiency and performance for microchip-based and capillary-based electrophoretic separation systems: a closer look *Electrophoresis* **25** 253–69

[33] Dash S and Mohanty S 2014 Dielectrophoretic separation of micron and submicron particles: a review *Electrophoresis* **35** 2656–72

[34] Kale A, Patel S, Hu G and Xuan X 2013 Numerical modeling of joule heating effects in insulator-based dielectrophoresis microdevices *Electrophoresis* **34** 674–83

[35] Modarres P and Tabrizian M 2017 Alternating current dielectrophoresis of biomacromolecules: the interplay of electrokinetic effects *Sensors Actuators* B **252** 391–408

[36] Prabhakaran R A, Zhou Y, Patel S, Kale A, Song Y, Hu G and Xuan X 2017 Joule heating effects on electroosmotic entry flow *Electrophoresis* **38** 572–9

[37] Rumble J R 2018 *CRC Handbook of Chemistry and Physics* 98th edn (Boca Raton, FL: CRC Press/Taylor & Francis)

[38] White H S and Bund A 2008 Ion current rectification at nanopores in glass membranes *Langmuir* **24** 2212–8

[39] Calander N 2009 Analyte concentration at the tip of a nanopipette *Anal. Chem.* **81** 8347–53

[40] Orelovitch O L, Apel P Y and Sartowska B 2006 New methods of track membrane treatment in the preparation of samples for further observation with scanning electron microscopy *J. Microsc.* **224** 100–3

[41] Saucedo-Espinosa M A and Lapizco-Encinas B H 2015 Experimental and theoretical study of dielectrophoretic particle trapping in arrays of insulating structures: effect of particle size and shape *Electrophoresis* **36** 1086–97

[42] Saucedo-Espinosa M A and Lapizco-Encinas B H 2015 Design of insulator-based dielectrophoretic devices: effect of insulator posts characteristics *J. Chromatogr.* A **1422** 325–33

[43] Sexton L T, Horne L P and Martin C R 2007 Developing synthetic conical nanopores for biosensing applications *Mol. BioSyst.* **3** 667–85

[44] Clarke R W, Piper J D, Ying L and Klenerman D 2007 Surface conductivity of biological macromolecules measured by nanopipette dielectrophoresis *Phys. Rev. Lett.* **98** 198102/1–4

[45] Clarke R W, White S S, Zhou D, Ying L and Klenerman D 2005 Trapping of proteins under physiological conditions in a nanopipette *Angew. Chem., Int. Ed. Engl.* **44** 3747–50

[46] Smith K J P, May M, Baltus R and McGrath J L 2017 A predictive model of separations in dead-end filtration with ultrathin membranes *Sep. Purif. Technol.* **189** 40–7

[47] Sonnefeld J 1996 Determination of surface charge density parameters of silicon nitride *Colloids Surf.* A **108** 27–31

[48] Siwy Z S 2006 Ion-current rectification in nanopores and nanotubes with broken symmetry *Adv. Funct. Mater.* **16** 735–46

[49] Bard A J and Faulkner L R 2001 *Electrochemical Methods: Fundamentals and Applications* (New York: Wiley) p 864

[50] Keesom W H, Zelenka R L and Radke C J 1988 A zeta-potential model for ionic surfactant adsorption on an ionogenic hydrophobic surface *J. Colloid Interface Sci.* **125** 575–85

[51] Molla S H and Bhattacharjee S 2005 Prevention of colloidal membrane fouling employing dielectrophoretic forces on a parallel electrode array *J. Membr. Sci.* **255** 187–99